IEEE Access
Multidisciplinary ⋮ Rapid Review ⋮ Open Access Journal

Received 5 January 2024, accepted 24 January 2024, date of publication 30 January 2024, date of current version 9 February 2024.

Digital Object Identifier 10.1109/ACCESS.2024.3360300

RESEARCH ARTICLE

A Novel Salp Swarm Optimization Oriented 3-DOF-PIDA Controller Design for Automatic Voltage Regulator System

NELSON DHANPAL CHETTY[1,2], GULSHAN SHARMA[2], (Member, IEEE), RAVI GANDHI[3], (Member, IEEE), AND EMRE ÇELIK[4]

[1]Department of Electrical Power Engineering, Durban University of Technology, Durban 4001, South Africa
[2]Department of Electrical Engineering Technology, University of Johannesburg, Johannesburg 2006, South Africa
[3]School of Engineering, Ajeenkya D. Y. Patil University, Pune 412105, India
[4]Department of Electrical and Electronics Engineering, Engineering Faculty, Düzce University, 81620 Düzce, Turkey

Corresponding authors: Ravi Gandhi (ravi.gandhi09@gmail.com) and Nelson Dhanpal Chetty (nelsonc@dut.ac.za)

ABSTRACT Voltage stability is critical in electrical power systems, and automatic voltage regulators play a crucial role in maintaining voltage levels within permissible limits. Due to their simplicity and effectiveness, traditional Proportional-Integral-Derivative (PID) controllers have been widely used in automatic voltage regulation. However, they may not always perform optimally in complex power systems with varying operating conditions and external disturbances. This research introduces an integrated approach of employing a 3-degrees of freedom-PID-Acceleration (3-DOF-PIDA) controller coupled with a disturbance observer-based control strategy. This combination is embedded with a simple but effective salp swarm optimisation algorithm. This novel control approach of the combined 3-DOF-PIDA, disturbance observer and salp swarm optimisation will enhance the voltage regulation of the system. The proposed novel control strategy incorporates an acceleration component to continuously adjust its parameters based on system dynamics. Simultaneously, the disturbance observer is responsible for estimating and compensating for external disturbances, further improving the system's performance. The salp swarm optimization is applied to optimize both the PIDA control parameters and the disturbance observer's parameters in the automatic voltage regulation system to find optimal solutions that improve voltage regulation and disturbance rejection capabilities. The results are established by performing statistical and graphical analyses with time-varying step load fluctuations, and under various system parameter variations. The results are validated by comparisons to five popular optimization algorithms found in the reviewed literature. The investigations demonstrate that this new proposed approach provides outstanding performance, in the presence of substantial system parameter fluctuations and uncertainties.

INDEX TERMS Disturbance observer, PIDA controller, salp swarm optimization, voltage regulation.

NOMENCLATURE

D	Dimensional vector.
$D_e(s)$	Estimated lumped disturbance.
$E(s)$	3-DOF-PIDA tracking error.
$F(s)$	3-DOF-PIDA parameter tuning function.
$G_a(s)$	Amplifier transfer function.
$G_d(t)$	Load disturbance.
$G_e(s)$	Exciter transfer function.
$G_g(s)$	Generator transfer function.
K_{ac}	Acceleration gain.
K_d	Derivative gain.
K_i	Integral gain.
K_l	Lumped disturbance gain.
K_p	Proportional gain.
N_a	Acceleration filter coefficient.
N_d	Derivative filter coefficient.
$R(s)$	3-DOF-PIDA reference voltage.

The associate editor coordinating the review of this manuscript and approving it for publication was Zhiguang Feng.

T_m	Maximum number of SOS iterations.
$U(s)$	3-DOF-PIDA control action.
$Y(s)$	3-DOF-PIDA sensor feedback.
dK_a	Change in amplifier gain.
dK_e	Change in exciter gain.
dK_g	Change in generator gain.
dK_s	Change in sensor gain.
dT_a	Change in amplifier time.
dT_e	Change in exciter time.
dT_g	Change in generator time.
dT_s	Change in sensor time.
$d(t)$	Lumped disturbance.
$e(t)$	Voltage error.
n	The random population of salps.
$r(t)$	AVR reference voltage.
$y(t)$	Generator output voltage,.
$y(t)$	Generator terminal voltage.
$z(t)$	Generator estimated state.
α	Proportional set-point coefficient.
β	Derivative set-point coefficient.
γ	Acceleration set-point coefficient.

I. INTRODUCTION

The change in the electrical energy environment and technological advancements have heightened the importance of voltage regulation in contemporary power systems. These systems are continually challenged by several factors, such as the constant increase in load demand, uncertainties in system parameters, dynamic changes in load, and the integration of erratic renewable energy sources. The importance of delivering consistent, high-quality electrical power is essential, emphasizing the need for stability and reliability in these advanced power systems.

Maintaining the integrity of power transmission and distribution networks and assuring the quality of electrical energy delivered to consumers depend on the ability to maintain voltage levels within predetermined limits [1]. By controlling the output voltage of generators, in reaction to load fluctuations and external disturbances, Automatic Voltage Regulation (AVR) systems are essential in reaching this goal [2]. The authors of [2] emphasize the real-world difficulties in designing and operating AVR systems. Due to its simplicity and efficiency in regulating voltage, PID controllers have historically been the pillar of AVR systems [3]. They are known for their rapid and precise voltage regulation, and their robustness in handling various operating conditions. However, it is pointed out in [4] that PID controller performance is often limited in the presence of external disturbances, nonlinearities in the system, and a wide range of operating circumstances. Advanced control strategies are required in these situations to improve voltage regulation capabilities by adapting to dynamic changes and disturbances [4].

An improvement of the traditional PID controller is the PIDA controller [5]. It has an acceleration component that constantly adjusts controller parameters, improving flexibility to shifting operating conditions and disturbances. In [5] the authors highlight the advantages of PIDA controllers, including their faster response times and increased accuracy compared to traditional PID controllers. As power systems become more complex, there is a need for increasingly sophisticated control procedures. By decoupling the acceleration mechanism from the PIDA controller, the 2-DOF-PID controller adds a new degree of freedom to the control structure [6]. This decoupling allows the acceleration component to be tuned more precisely, improving the performance and reliability of the controller. By adding a third DOF, a 3-DOF-PID controller, as suggested in [7], goes a step further and allows for the simultaneous adjustments of proportional, integral, derivative, and acceleration gains, which enables the controller to respond to complex power system dynamics with greater flexibility and precision. In [8] the authors show that the 3-DOF-PID controller performs better in a multi-area power system compared to the PID controller and the 2-DOF-PID controller.

The integration of a DOB into the 3-DOF-PIDA control framework is a significant progression for AVR systems. A comprehensive review of DOBs is offered in [9], with an emphasis on their use in nonlinear systems. The authors of [9] highlight the versatility of DOBs in managing a wide range of disturbances encountered in real-world power systems. Observer-based control strategies were employed in [10], [11], and [12] to estimate and reject both matched and mismatched types of lumped disturbances, which include load variations, nonlinearities, and uncertainties, in AVR systems. By incorporating a DOB, the 3-DOF-PID controller gains the capability to detect and react to disturbances in real-time, thereby enhancing the system's disturbance rejection capabilities [13].

The use of optimization algorithms to improve AVR controllers is a major advancement in voltage regulation. The need for more flexible and efficient control strategies has grown exponentially, as contemporary power systems deal with increased complexities, varying generation technologies and evolving demand patterns. Recent studies and comparative analyses have explored a wide range of Intelligence Base Algorithms, and heuristic and metaheuristic optimization techniques, which are employed in AVR systems [2], [4], [5], [6], [7], [8], [12], [13], [14], [15], [16], [17], [18], [19], [20], [21], [22], [23], [24], [25], [26], [27]. Some of the prevalent algorithms in the literature include the Bat Algorithm (BA), Fruit Fly (FFA), Whale Optimization Algorithm (WOA), Harmony Search (HAS), Grey Wolf Algorithm (GWA), Monarch Butterfly Algorithm (MBA), Ant Colony (ACO), Dragonfly (DFO), Cuckoo Search (CSO), Moth Flame Optimization (MFO), Artificial Bee Colony (ABC), Grasshopper Optimisation Algorithm (GOA) the Genetic Algorithm (GA), Tabu Search (TSA), Water Cycle Algorithm (WCA), Local Unimodal Sampling (LUS), as well as several adaptations and modifications of the Particle Swarm Optimization (PSO), and Teaching and Learning Based

Algorithms (TLBA) [2], [4], [5], [6], [7], [8], [12], [13], [14], [15], [16], [17], [18], [19], [20], [21], [22], [23], [24], [25], [26], [27], [28], [29], [30], [31], [32], [33], [34]. These algorithms provide adaptable and flexible optimization capabilities, enabling systematic exploration of control parameter spaces, and ensuring that controllers are optimized across a wide range of operating conditions. By using the potential of optimisation techniques, AVR controllers can adjust to dynamic changes in load demands, disturbances, and fluctuations in system parameters. This adaptability contributes to enhanced stability and reliability in the ever-evolving environment of modern power systems [12], [13], [14], [15], [16], [17], [18], [19], [20], [21], [22], [23], [24], [25], [26], [27], [28], [29], [30], [31], [32], [33], [34]. Heuristic optimization methods can adjust to a variety of control circumstances and system types, making them apt for systems with nonlinear dynamics or indeterminate parameters [31], [32]. Their conceptual simplicity and computational efficiency make them suitable for real-time control applications. Metaheuristic optimisation techniques are recognized for their proficiency in effectively identifying near-optimal solutions across a wide range of problem domains [33], [34].

The selection of an efficient optimization method is crucial in AVR control systems. There must be a balance between the benefits of optimization and the potential obstacles such as increased complexity, longer computation times, and additional costs. The SSO, is an effective optimization method to provide such features [35], [36], [37], [38], [39], [40], [41], [42], [43]. In-depth reviews of the SSO are presented in [35] and [36]. The effectiveness of a multi-objective SSO is illustrated in [37], where it is compared with the DFO algorithm, the GOA and the ant lion optimiser. The SSO's application in determining the optimal PID controller parameters of the AVR system is discussed in [38], where the analysis of transient response indicates that the SSO exhibits superior tuning capabilities and efficiency in enhancing the step response of an AVR system, outperforming the Ziegler-Nichols traditional tuning method and the ABC algorithm. However, the robustness or sensitivity of the proposed technique was not explored, and only a single test analysis was performed to assess the effectiveness of the SSO. The use of the SSO in tuning a fractional-order PID controller (FoPID) in the AVR system is investigated in [39]. The authors contrast the performance of the SSO-tuned controller with a PSO controller and the ABC-tuned controller, emphasizing the effectiveness of the SSO. In [40], the SSO-based FoPID tuning method for AVR systems outperforms the SSO-tuned PID controller in terms of disturbance rejection capabilities. However, the research does not demonstrate the effectiveness and efficiency of the proposed method in comparison with other contemporary tuning methods. The transient response analysis in [41] reveals that the SSO-PID outperforms the WCO-based PID controller. The findings in [42] corroborate the superior performance of the SSO compared to the GOA and the collective decision optimisation algorithm in a multi-area power system.

The benefits of an enhanced SSO are highlighted in [44]. The authors in [45] demonstrate the dominance of an advanced SSO when compared to the MFO algorithm, a refined HSA and the GA. The strengths of the SSO are merged with the PSO in [46]. A range of SSO modifications and adaptations are detailed in [26] and [47]. Despite the proven efficacy of the proposed advancements in [26], [44], [45], [46], and [47], there are no discussions on the computational complexities of these strategies, which poses challenges for their application in real-world AVR control systems.

The strength of the SSO lies in its simplicity to ensure excellent tuning of optimal control parameters. The SSO takes inspiration from the behaviour of salp chains [43]. These chains can adapt and navigate towards a continuously changing optimal solution (food source), thereby exploring, and exploiting the defined search space for better solutions. The unique features of the SSO that differentiate it from other optimization algorithms as per [43] are:

(*a*) The algorithm keeps the best solution found after each iteration, assigning it to the global optimum (food source) variable. This ensures the preservation of the best solution, even if the entire population declines.

(*b*) The SSO adjusts the position of the leading salp in relation to the food source, which is the best solution currently identified. This enables the leader salp to continuously explore and exploit its surroundings for improved solutions.

(*c*) The SSO adjusts the position of follower salps relative to each other, allowing them to gradually move towards the leading salp.

(*d*) The slow movements of follower salps prevent the SSO from getting trapped in local optima, and the adaptive mechanism allows it to accurately estimate the best solution while continuously avoiding entrapment in local solutions.

(*e*) The SSO has a single control parameter which is adaptively decreased over iterations, assisting the algorithm in initially exploring the search space and exploiting it towards the end, thus simplifying its implementation and reducing the complexity.

These advantages position the SSO as a potentially superior solution for optimization problems compared to traditional methods and computationally complex approaches, which is the motivation for the current research. Balancing the benefits of optimization with the added complexity and increased computational times is a significant consideration in AVR systems. The SSO is conceptually simple and computationally efficient, making it suitable for real-time control applications. The relevant literature confirms that the combined approach of embedding the SSO with a 3-DOF-PIDA and a DOB, to configure a unified AVR control approach, has not been previously investigated. Hence, this research paper investigates the performance of a 3-DOF-PIDA controller combined with a standard DOB and embedded with an SSO in the AVR control system. The SSO is used to optimize the parameters of the 3-DOF-PIDA controller and the DOB, ensuring they work in harmony to

achieve enhanced disturbance rejection and precise voltage regulation. Together, they aim to provide superior voltage regulation performance by addressing dynamic operating conditions and external disturbances which improves disturbance rejection, adaptability, and robustness in control systems, making this combination a valuable tool in AVR applications. Considering the above, the dynamics and modelling of AVR control systems using MATLAB 2023 software, the following are the significant contributions of the current work:

- To estimate the total effect of various irregularities, parametric uncertainties, and load disturbance for the generator dynamics as a single lumped disturbance.
- To develop the disturbance rejection structure using the information from the DOB for the AVR system and to evaluate the performance of the AVR under several considered cases. Unlike the work presented in [12], here, only one DOB is utilized to estimate and compensate for the effect of the lumped disturbance from the generator dynamics.
- Most of the controllers designed for AVR systems have a 1-DOF or 2-DOF PID control structure. In [28], a 3-DOF PID controller is proposed using the feed-forward compensation method for the load disturbance only. However, such a controller may not be capable of compensating for the total effect of various irregularities, parametric uncertainties, and load disturbance [10], [11]. Hence, in this paper, a novel 3-DOF PID plus Acceleration (i.e., PIDA) controller is proposed to enhance the performance and robustness of the AVR system.
- The simulation results of the SSO-integrated 3-DOF-PIDA controller are compared with five popular AVR control strategies with detailed graphical and analytical analyses.

The subsequent sections of this paper provide the theoretical foundations of AVR systems, the integration of a single Extended State Observer (ESO) based DOB into the AVR system, the 3-DOF-PIDA controller, and the utilization of the SSO for parameter optimization. Simulated results and comparative analyses are presented and compared to five other controller designs that are popular in the relevant literature, namely, WOA-PIDA [21], TLBO-PIDA [27], LUS-PIDA [25], HAS-PIDA [22], and BAT-PIDA [19], to demonstrate the effectiveness of the proposed novel approach in improving voltage regulation.

II. DYNAMICS OF THE AVR

AVR, a critical component in power systems, is responsible for maintaining a consistent, stable, and desired voltage level at the generator's terminals. The primary function of the AVR is to regulate the generator's field excitation to control the output voltage within acceptable limits, under varying load conditions and disturbances.

The operation of the AVR is explained in [1], [28], [29], and [30]. Fig. 1 shows the basic components of an AVR system. The AVR continuously monitors the generator's output voltage, $y(t)$ via sensor feedback, and the difference between the reference voltage, $r(t)$ and the actual terminal voltage, $y(t)$ is calculated to determine the voltage error, $e(t)$. This signal is applied to the amplifier with a transfer function, $G_a(s)$. To minimize the voltage error and maintain the terminal voltage within a specified range, the exciter of the AVR generates a control signal with a transfer function, $G_e(s)$ that adjusts the field voltage applied to the generator's rotor or field winding. The generator field can be represented by a block with a transfer function, $G_g(s)$. The generator's excitation level is controlled by the field voltage, which impacts the terminal voltage. By adjusting the field voltage, the AVR controls the magnetic field strength within the generator, affecting the electromotive force (EMF) induced in the stator windings. This, in turn, regulates the terminal voltage to maintain it at or near the desired reference level.

The AVR constantly responds to changes in the electrical load, $V_d(t)$, ensuring that the terminal voltage remains stable. When load variations occur, the AVR quickly adjusts the field excitation to counteract voltage drops or spikes, maintaining system stability and the quality of the supplied power. The mathematical model of an AVR is developed by [1]. The amplifier, exciter, generator, and sensor with parametric uncertainties: $K_a, dK_e, dK_g, dK_s, dT_a, dT_e, dT_g, dT_s$, within the ranges shown in Table 1, can be approximated by (1)-(4) [12].

$$G_a(s) = \frac{K_a + dK_a}{(T_a + dT_a)s + 1} \tag{1}$$

$$G_e(s) = \frac{K_e + dK_e}{(T_e + dT_e)s + 1} \tag{2}$$

$$G_g(s) = \frac{K_g + dK_g}{(T_g + dT_g)s + 1} \tag{3}$$

$$G_s(s) = \frac{K_s + dK_s}{(T_s + dT_s)s + 1} \tag{4}$$

Using (1)-(4), the AVR state-space model with load disturbance, $G_d(t)$ including parametric uncertainties, and nonlinearities in the generator dynamics are described by (5)-(7). Where, $x(t) = [V_g(t)\, V_e(t)\, V_a(t)]$, $u(t) = V_c(t)$, and $y(t) = V_g(t)$, as the state, input, and output vectors, respectively [12].

$$\dot{x}_1(t) = -\left(\frac{1}{T_g}\right)x_1(t) + \left(\frac{K_g}{T_g}\right)x_2(t) + \left(\frac{-V_d - \dot{V}_d\left(T_g + dT_g\right) + dK_g x_2(t) - \dot{x}_1(t)\, dT_g}{T_g}\right) \tag{5}$$

$$\dot{x}_2(t) = -\left(\frac{1}{T_e}\right)x_2(t) + \left(\frac{K_e}{T_e}\right)x_3(t) \tag{6}$$

$$\dot{x}_3(t) = -\left(\frac{1}{T_a}\right)x_3(t) + \left(\frac{K_a}{T_a}\right)u(t) \tag{7}$$

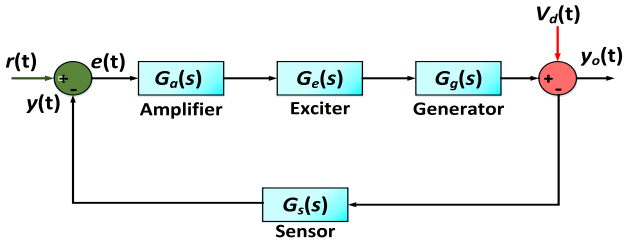

FIGURE 1. Block Diagram of an AVR System.

TABLE 1. Description of AVR components and their ranges [1].

AVR Components	Gain	Time
Amplifier	$10 \leq K_a \leq 40$	$0.02 \leq T_a \leq 0.1$
Exciter	$1 \leq K_e \leq 10$	$0.4 \leq T_e \leq 1$
Generator	$0.7 \leq K_g \leq 1$	$1 \leq T_g \leq 2$
Sensor	$K_s = 1$	$0.001 \leq T_s \leq 0.06$

Were, these dynamics with lumped disturbance, $d(t)$ in the standard state-space model by (8)-(10).

$$\dot{x}(t) = \begin{bmatrix} -a_1 & b_1 & 0 \\ 0 & -a_2 & b_2 \\ 0 & 0 & -a_3 \end{bmatrix} x(t) + \begin{bmatrix} 0 \\ 0 \\ b_3 \end{bmatrix} u(t) + \begin{bmatrix} 1 \\ 0 \\ 0 \end{bmatrix} d(t) \tag{8}$$

$$y(t) = \begin{bmatrix} 1 & 0 & 0 \end{bmatrix} x(t) \tag{9}$$

$$d(t) = \frac{-V_d - \dot{V}_d \left(T_g + dT_g\right) + dK_g x_2(t) - \dot{x}_1(t) dT_g}{T_g} \tag{10}$$

III. DYNAMICS OF DOB

The DOB serves as a valuable component of the AVR control system. The disturbance captures the total effect of irregularities like parametric uncertainties, nonlinearities, and external load disturbances which are commonly referred to as lumped disturbances [9]. The detailed model of the AVR along with the lump disturbance, $d(t)$ in the generator component is presented by (8)-(10). Based on (5)-(7), it is observed that, $d(t)$ is a mismatched type of lumped disturbance [9]. It is demonstrated that the estimator and controller design, for tackling mismatched disturbances in real-time systems akin to AVR is challenging [11], [12]. In this paper, a single ESO approach is used, from the MESOBC method presented in [10]. The overall generator dynamics with lumped disturbance can be represented by (11) [10]:

$$\left.\begin{aligned} \dot{x}_1(t) &= -a_1 x_1(t) + b_1 x_2(t) + d(t) \\ y(t) &= x_1(t) \end{aligned}\right\} \tag{11}$$

The voltage of the exciter $x_2(t)$ can be used as an input using the proper sensor for (11). Using the MESO methodology, the lumped disturbance $d(t)$ is considered as an extended state. The new state variables are formed as follows:

$$\left.\begin{aligned} z_1(t) = x_1(t) \text{ and } z_2(t) &= d(t) \\ \bar{u}(t) &= x_2(t) \\ \bar{y}(t) &= z_1(t) \end{aligned}\right\} \tag{12}$$

Combining (11) and (12), under the assumptions mentioned in [10], the estimated states of the generator model are presented in (13):

$$\left.\begin{aligned} \dot{\hat{z}}_1(t) &= -a_1 \hat{z}_1(t) + \hat{z}_2(t) + b_1 \bar{u}(t) + l_1 (z_1(t) - \hat{z}_1(t)) \\ \dot{\hat{z}}_2(t) &= l_2 (z_1(t) - \hat{z}_1(t)) \end{aligned}\right\} \tag{13}$$

Considering, $e_1(t) = z_1(t) - \hat{z}_1(t)$, and $e_2(t) = z_2(t) - \hat{z}_2(t)$, the first derivative of the estimation error vector, $e(t) = \begin{bmatrix} e_1(t) \\ e_2(t) \end{bmatrix}$ using (13) can be given by (14).

$$\dot{e}(t) = \begin{bmatrix} -a_1 - l_1 & 1 \\ 0 & -l_2 \end{bmatrix} e(t) + \begin{bmatrix} 0 \\ 1 \end{bmatrix} \dot{d}(t) \tag{14}$$

Finally, if $L = \begin{bmatrix} l_1 \\ l_2 \end{bmatrix}$ is chosen in such that, $\begin{bmatrix} -a_1 - l_1 & 1 \\ 0 & -l_2 \end{bmatrix}$ remains Hurwitz then the estimation error dynamics of ESO in (14) converges asymptotically [9], [10]. To solve this problem, single frequency, w_l can be chosen such that, $l_1 = 2w_l - a_1$ and $l_2 = w_l^2$.

IV. STRUCTURE OF THE SSO-3-DOF-PIDA CONTROLLER

The next objective is to minimize the effect of the lumped disturbances using the DOB estimated disturbance, $\boldsymbol{d_e(t)}$. It is the prime objective of the AVR control system to maintain the generator's terminal voltage close to the reference voltage, $\boldsymbol{r(t)}$. Hence, for stability advancement, response enhancement and disturbance rejections, various PID controllers have been used including FoPID, 2-DOF-PID, 3-DOF-PID, etc. [7], [8], [17], [18].

However, an additional term called "Acceleration" has been introduced with the PID controllers that improve the speed of response and increase the stability margin compared with the PID controllers. This is commonly known as a PIDA controller [32], [33], [34]. The control action delivered by the PIDA controller is given as a function of a tracking error by, $E(s) = R(s) - Y(s)$ which may be expressed by (15)-(16) with the ten 3-DOF-PIDA controller optimisation parameters defined in Table 2.

$$\begin{aligned} U(s) = K_p [R(s) - Y(s)] + \frac{K_i}{s} [R(s) - Y(s)] \\ + K_d s [R(s) - Y(s)] + K_{ac} s^2 [R(s) - Y(s)] \end{aligned} \tag{15}$$

$$U(s) = K_p [E(s)] + \frac{K_i}{s} [E(s)] + K_d s [E(s)] + K_{ac} s^2 [E(s)] \tag{16}$$

This section introduces a new structure of a PIDA controller with an embedded DOB and a SSO based parameter tuning mechanism as shown in Fig. 2.

A. STRUCTURE OF THE 3-DOF-PIDA CONTROLLER

The structure of the proposed 3-DOF-PIDA controller is shown in Fig. 3 using the Laplace domain. It is composed of three inputs; $R(s)$, $Y(s)$, and $D_e(s)$, and one control output; $U(s)$. Here, $R(s)$ is the reference voltage, $Y(s)$ denotes

TABLE 2. Description of SSO-3-DOF-PIDA parameters.

Symbol	Description	Symbol	Description
K_p	Proportional gain	α	Proportional set-point coefficient
K_i	Integral gain	β	Derivative set-point coefficient
K_d	Derivative gain	γ	Acceleration set-point coefficient
K_{ac}	Acceleration gain	N_d	Derivative filter coefficient
K_l	Lumped disturbance gain	N_a	Acceleration filter coefficient

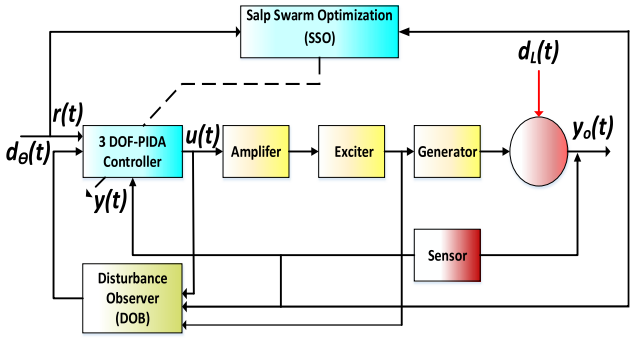

FIGURE 2. Model of an AVR system with the inclusion of SSO-3-DOF-PIDA controller and with DOB.

the sensor feedback from the output of the power system, $D_e(s)$ dotes the estimated lumped disturbance in the generator dynamics. The control action is presented by $U(s)$.

As shown in Fig. 3, the controller output can be expressed as a function of 3-input signals as follows:

$$\begin{aligned} U(s) &= K_p[\alpha R(s) - Y(s)] + \frac{K_i}{s}[R(s) - Y(s)] \\ &\quad + K_d\left(\frac{N_d s}{s+N_d}\right)[\beta R(s) - Y(s)] \\ &\quad + K_{ac}\left(\frac{N_a s}{s+N_a}\right)^2[\gamma R(s) - Y(s)] + K_l D_e(s) \end{aligned} \tag{17}$$

$$\begin{aligned} U(s) &= \left[\alpha K_p + \beta K_d\left(\frac{N_d s}{s+N_d}\right) + \gamma K_{ac}\left(\frac{N_a s}{s+N_a}\right)^2 + \frac{K_i}{s}\right] R(s) \\ &\quad - \left[K_p + K_d\left(\frac{N_d s}{s+N_d}\right) + K_{ac}\left(\frac{N_a s}{s+N_a}\right)^2 + \frac{K_i}{s}\right] Y(s) \\ &\quad + [K_l] D_e(s) \end{aligned} \tag{18}$$

It is observed from (17) that the control output, $U(s)$, is not the direct function of the tracking error, $E(s)$ but an integral component thereof. The set-point coefficients, α, β, and γ are multiplied with the proportional, derivative and acceleration terms respectively. These constants help in

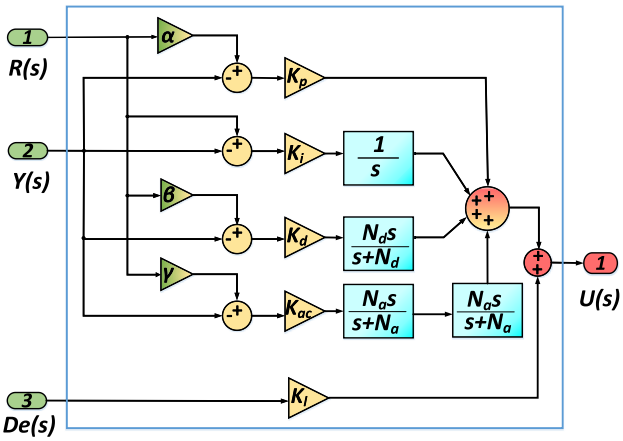

FIGURE 3. Structure of the 3-DOF-PIDA Controller.

tracking the desired terminal voltage levels, thus improving the transient and steady-state performances of the generator. Also, the first-ordered derivative filter and second-ordered acceleration filter with filter coefficients of, N_d and, N_a respectively, are introduced to handle the derivative kick and low frequency noise. Lastly, K_l is integrated with the DOB estimated disturbance, $D_e(s)$ to minimize the effect of the lumped disturbance.

The effectiveness of the 3-DOF component can be seen from another representation of the control action, $U(s)$ as shown in (19):

$$U(s) = F_1(s)R(s) + F_2(s)Y(s) + F_3 D_e(s) \tag{19}$$

Were,

$$F_1(s) = \alpha K_p + \beta K_d\left(\frac{N_d s}{s+N_d}\right) + \gamma K_{ac}\left(\frac{N_a s}{s+N_a}\right)^2 + \frac{K_i}{s} \tag{20}$$

$$F_2(s) = K_p + K_d\left(\frac{N_d s}{s+N_d}\right) + K_{ac}\left(\frac{N_a s}{s+N_a}\right)^2 + \frac{K_i}{s} \tag{21}$$

$$F_3(s) = K_l \tag{22}$$

The three terms, $F_1(s)$, $F_2(s)$ and $F_3(s)$, shown in (20)-(22), which are functions of the tuning parameters, are multiplied with the reference input, $R(s)$ the terminal output, $y(s)$ and the estimated lumped disturbance, $D_e(s)$ respectively. Hence, the proposed control structure has 3-Degrees of Freedom (DOF) compatibility to provide set-point tracking, disturbance rejection and robust performance. These 10 parameters are optimized using the Integral Time-weighted Square Error (ITSE) criterion-based SSO. The optimized values and their ranges are summarized in the Appendix.

B. SALP SWARM OPTIMIZATION (SSO)

The SSO is a bio-inspired optimization algorithm that draws inspiration from the collective behavior of salps, which are marine filter-feeding organisms. In recent years, the SSO has gained recognition as a potent tool for optimizing

complex systems, particularly in the field of control engineering [35], [36], [37], [38], [39], [40], [41], [42], [43]. The SSO algorithm begins by initializing a population of virtual salps within the solution space, each representing a potential set of control parameters for the AVR system. This population reflects the diversity of potential solutions.

The core of the SSO's operation lies in evaluating the fitness or objective function for each salp's position, quantifying the quality of the corresponding solution in optimizing the AVR system's parameters. The evaluation serves as the basis for decision-making. Salps make decisions based on a blend of exploitation and exploration tendencies. They are influenced by the positions of the best solutions they have encountered (exploitation) and the positions of other well-performing salps (exploration).

The algorithm's success hinges on effectively balancing these two aspects. Salps iteratively update their positions and solutions based on the movement rules and fitness function evaluations. As the optimization progresses, salps gradually converge toward optimal or near-optimal control settings for the AVR system. The algorithm continues until a predefined termination criterion is met. Common termination criteria include reaching a maximum number of iterations or achieving a specified level of solution quality. The mathematical representation of the movement of salps in the SSO can be expressed as follows; The initialization of the algorithm starts by generating a random population of, 'n' salps, in the 'D' dimensional vector.

$$x\,(i) = [x_i 1, x_i 2, x_i 3 \ldots\ldots, x_i D] \quad \forall i = 1, 2, 3 \ldots, n \quad (23)$$

Were, D is the dimension of decision variables. The spatial coordinates of all the salps are verified within a two-dimensional matrix referred to as, 'x'. Further, a specified food source denoted as, 'F' is presumed to be the target, within the exploration area of the swarm. The SSO parameters are defined in Table 3. The leader position is presented in (24) [43]:

$$x_j = \begin{cases} F_j + c_1 \left(\left(UB_j - LB_j\right) c_2 + LB_j\right)\right) c_3 \geq 0 \\ F_j - c_1 \left(\left(UB_j - LB_j\right) c_2 + LB_j\right)\right) c_3 < 0 \end{cases} \quad (24)$$

TABLE 3. Description of SSO parameters.

Symbol	Description
x_j	position of *leader* in, j^{th} dimension
F_j	*leader* position in, j^{th} dimension.
UB_j	upper bound of j^{th} dimension
LB_j	lower bound of j^{th} dimension
$c_1, c_2, \& c_3$	random numbers

The effectiveness of the SSO in the exploration and exploitation of food is shaped by, c_1, and may be presented as (25) [43]:

$$c_1 = 2e^{-\frac{4l}{T_m}} \quad (25)$$

Were, T_m represents the maximum number of iterations and 'l' represents the current iteration. c_2, & c_3 are random numbers generated during the iteration process. The follower's position is instantly updated and given by (26) [43]:

$$x_j^n = \frac{1}{2}\left(x_j^n + x_j^{n-1}\right) \forall n \geq 28 \quad (26)$$

x_j^n is the position of n^{th} follower in j^{th} dimension. If a salp moves beyond the defined search space, it is rapidly substituted with a new solution chosen at random. This guarantees that the replacement solution is confined within the search space boundaries. The algorithm stops upon reaching the designated maximum iteration count or when specific pre-defined criteria are met. The execution flowchart of the SSO is provided in Fig. 4.

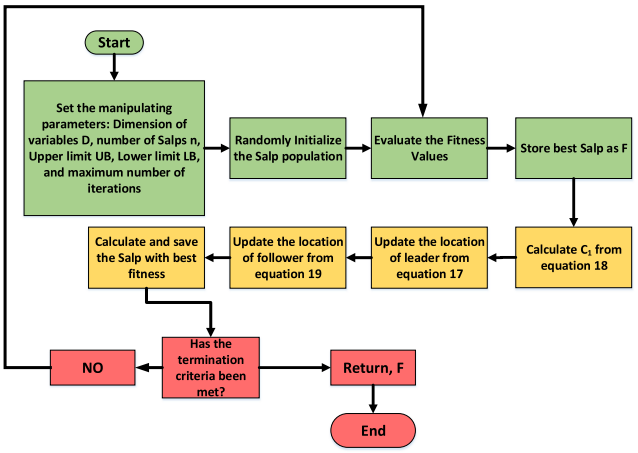

FIGURE 4. The flowchart of the SSO execution process.

V. RESULTS AND ANALYSIS

The mathematical modelling of the AVR, the 3-DOF-PIDA, the DOB, and the SSO is presented in the previous sections of this paper. In the investigations and simulations, the Integral Time-weighted Squared Error (ITSE) is chosen as the objective function to minimize the error of the system and to obtain an improved output of the AVR using the proposed SSO-3-DOF-PIDA regulator as shown in (27):

$$J = \int_{t_0}^{t_f} \left[(r\,(t) - y(t))^2 \times t\right] dt \quad (27)$$

Were,

$r(t) = Reference\ voltage$
$y(t) = Terminal\ output\ voltage$

The performance of the SSO-3-DOF-PIDA, under various considered cases, is compared with five other controller designs that are popular in the reviewed literature, namely, WOA-PIDA, TLBO-PIDA, LUS-PIDA, HAS-PIDA, and BAT-PIDA. From Table 1, the AVR simulation parameters are:

$K_a = 10, K_e = 1, K_g = 1, K_s = 1, T_a = 0.1, T_e = 0.4, T_g = 1, T_s = 0.01$, with the applicable units. Using these simulation parameters, the AVR, state-space matrices are given by (28).

$$A = \begin{bmatrix} -1 & 1 & 0 \\ 0 & -2.5 & 2.5 \\ 0 & 0 & -10 \end{bmatrix},$$
$$B = \begin{bmatrix} 0 \\ 0 \\ 100 \end{bmatrix}, \quad C = \begin{bmatrix} 1 & 0 & 0 \end{bmatrix} \tag{28}$$

The pair of, $(A\&B)$ is controllable and the pair, $(A\&C)$ is observable [10]; hence the control design is further investigated. To achieve optimal and robust performance against lumped disturbances, the main components of the AVR system; amplifier; exciter; generator; with sensor are incorporated into the design. The performance of the SSO-3-DOF-PIDA is first evaluated and compared under normal conditions and the output of the proposed AVR, with the inclusion of the DOB using the ESO structure, is compared with the following popular optimization AVR designs; WOA-PIDA, TLBO-PIDA, LUS-PIDA, HAS-PIDA, and BAT-PIDA.

Fig. 5 illustrates the convergence profile of the SSO during the minimization of the ITSE value, with a set maximum iteration number of 100. The graph indicates a notable initial decrease in the ITSE value, followed by a consistent reduction without undesirable oscillations. This suggests that the SSO demonstrates promising convergence characteristics. Notably, from Fig. 5 it is observed that the algorithm stagnated and reached the final solution within 40–50 iterations. Subsequent iterations did not yield further improvement in the ITSE value. This supports the decision to limit the maximum iteration to 100 for the current study.

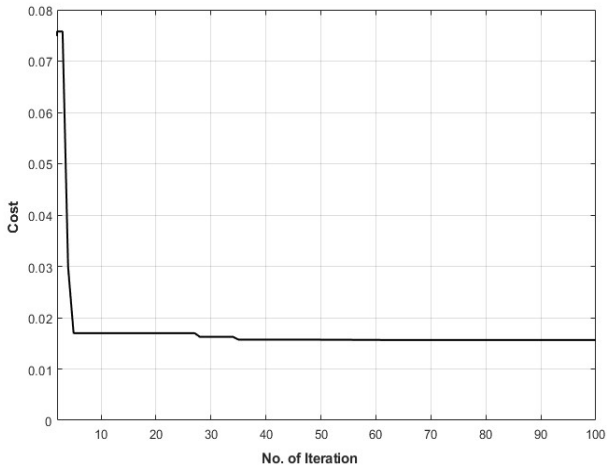

FIGURE 5. Convergence response of cost function (ITSE) with respect to number of iterations.

The graphical result for the terminal voltage is shown in Fig. 6 and the analytical results are given in Table 4. Thereafter, the performance of the SSO-3-DOF-PIDA is evaluated

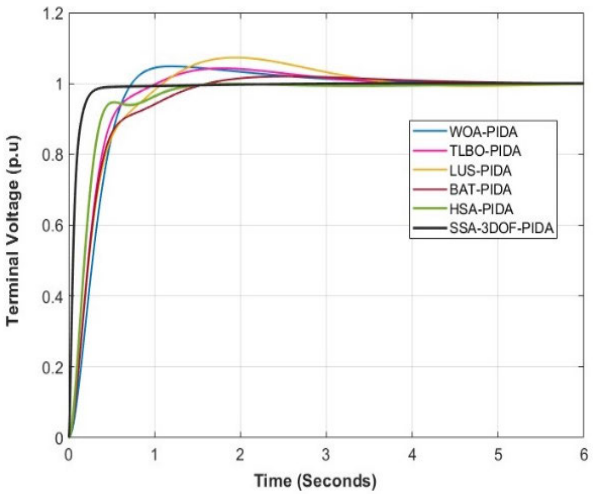

FIGURE 6. Response of terminal voltage under normal conditions.

TABLE 4. Dynamic response specification of AVR with normal condition.

Method	Overshoot / Undershoot (%)	Peak Value (p.u)	Rise Time (Seconds)	ITSE
WOA-PIDA [21]	1.6	1.016	0.54	0.01651
TLBO-PIDA [27]	1.0	1.01	1.35	0.01205
LUS-PIDA [23]	3.2	1.032	1.23	0.01636
HAS-PIDA [23]	0.4	0.996	1.35	0.01425
BAT-PIDA [18]	0.1	1.0010	2.05	0.01616
SSO-3-DOF-PIDA	0.07	1.0007	0.4	0.00130

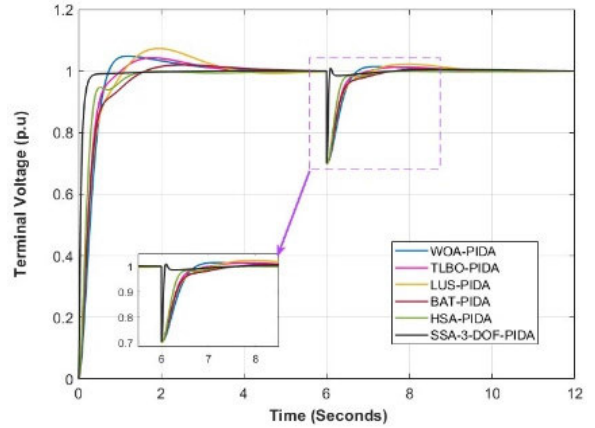

FIGURE 7. Response of terminal voltage under +30% step change in load voltage.

and compared under 30% step load voltage variation. The graphical result for the terminal voltage is shown in Fig. 7 and the analytical performance is given in Table 5.

It is observed, in Fig. 6, that the terminal voltage deviates with overshoot and is unable to promptly settle to refer-

TABLE 5. Dynamic response specification of AVR under +30% step load voltage variation.

Method	Peak Overshoot / Undershoot (%)	Peak Value (p.u)	Recovery Time (Seconds)	ITSE
WOA-PIDA [21]	1.65	1.0165	0.55	0.10861
TLBO-PIDA [27]	1.00	1.0100	0.45	0.08906
LUS-PIDA [23]	3.20	1.0320	1.23	0.09782
HAS-PIDA [23]	0.05	0.9995	1.5	0.09725
BAT-PIDA [18]	0.10	1.0010	1.45	0.09675
SSO-3-DOF-PIDA	1.00	1.0100	0.08	0.01859

ence value for the WOA-PIDA, TLBO-PIDA, LUS-PIDA, and BAT-PIDA, while the HAS-PIDA does not display any overshoot and has a quicker settling time of approximately 1.5 seconds compared to the other four controllers which take approximately 4.0 seconds to reach the reference voltage. The SSO-3-DOF-PIDA returns to the 1.0 p.u. terminal voltage within 0.5 seconds with no overshoot and without any oscillations. The SSO-3-DOF-PIDA stands out as the top performer, offering no overshoot, fast response, and excellent steady-state control.

From Table 4, it is noted that the SSO-3-DOF-PIDA exhibits the fastest transient response with the shortest rise time of 0.4 seconds. It outperforms the other five methods in terms of response speed. The BAT-PIDA and HAS-PIDA have low peak overshoots of 0.1% and 0.4%, indicating a smooth response with minimal overshoot. The TLBO-PIDA, WOA-PIDA, and LUS-PIDA have irregular responses with noticeable overshoot as indicated by the overshoot values 1.0%, 1.6%, and 3.2% respectively. The SSO-3-DOF-PIDA performs exceptionally well with an extremely low peak overshoot of 0.07%. The SSO-3-DOF-PIDA has the lowest ITSE value of 0.001308, implying excellent steady-state control and negligible error accumulation over time, compared to the other five methods. The WOA-PIDA and the HAS-PIDA balance peak overshoot combined with response speed well, making them suitable for applications requiring quick response with minimal overshoot. The BAT-PIDA performs well in terms of smoothness but sacrifices response speed. The TLBO-PIDA and LUS-PIDA offer smoother responses but with slightly longer rise times. The SSO-3-DOF-PIDA excels in terms of speed, precision, and low overshoot, making it suitable for applications demanding high-performance voltage regulation.

It is demonstrated in Fig. 7 that the SSO-3-DOF-PIDA is much faster and more accurate with minimal overshoot in reaching the SS error to zero after the voltage is varied +30% from the reference value. From Table 5, it is observed that the HAS-PIDA and BAT-PIDA have the lowest peak overshoots, both at 0.05% and 0.10% respectively, implying minimal deviations from the desired voltage responses during the transient period. While the WOA-PIDA, TLBO-PIDA, and SSO-3-DOF-PIDA have moderate peak overshoots, with values ranging from 1.00% to 1.65%. The LUS-PIDA exhibits the highest peak overshoot value of 3.2%, and peak value of 1.0320 p.u, indicating a significant deviation from the desired voltage response and a higher peak voltage during the transient period. The HAS-PIDA has the lowest peak value of 0.9995 p.u, suggesting a conservative response. The other five controllers, including the SSO-3-DOF-PIDA, have peak values close to 1.0100 p.u indicating a well-controlled response.

The LUS-PIDA, BAT-PIDA, and HAS-PIDA have recovery times of 1.23 seconds, 1.45 seconds, and 1.5 seconds respectively, indicating much slower recovery times. The TLBO-PIDA and WOA-PIDA show fast recovery times of 0.45 seconds and 0.55 seconds respectively. However, the SSO-3-DOF-PIDA stands out with the shortest recovery time of 0.08 seconds, indicating a rapid return to the desired voltage level, and it also has the lowest ITSE value of 0.01859, indicating superior steady-state performance with negligible error accumulation. The other five controllers have ITSE values close to 0.1, implying good steady-state control.

The HAS-PIDA and BAT-PIDA provide moderate responses with minimal overshoot and are suitable for applications where overshoot needs to be minimized while the LUS-PIDA exhibits higher overshoot and longer recovery time. The TLBO-PIDA offers good overall performance with a moderate recovery time and ITSE value. However, the SSO-3-DOF-PIDA offers rapid recovery and excellent steady-state performance.

Fig. 8 shows the response of the DOB under +30% step change in load voltage, and it is clear from the response that the DOB can track the actual load disturbance and is hence capable of improving the dynamic performance of the proposed AVR system.

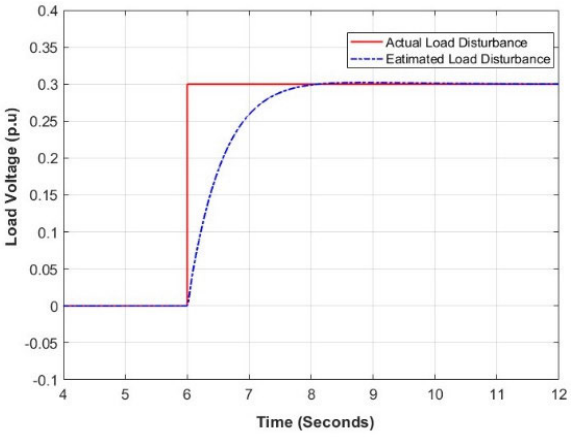

FIGURE 8. Response of Disturbance Observer under +30% step change in load voltage.

Fig. 9 shows the graphical response of the terminal voltage and the DOB under multi-step change in load voltage with

the SSO enhanced 3-DOF-PIDA controller and it is revealed that the DOB can track the actual disturbance and there is not much difference between actual and estimated disturbance and hence the SSO optimized 3-DOF-PIDA is successful in minimizing peak overshoot/undershoot, improving the settling time and eliminating the steady state error from the AVR response under multi-step change in the load voltage.

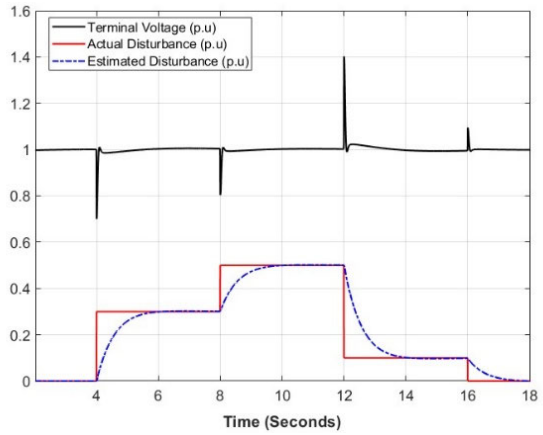

FIGURE 9. Response of terminal voltage and Disturbance Observer under a multi-step change in load voltage with SSO-enhanced 3-DOF-PIDA Controller.

A sensitivity analysis is conducted to determine the robustness of the SSO-3-DOF-PIDA-based AVR system. This is achieved by changing the time constants of the amplifier (T_a), exciter (T_e), generator (T_g), and the system sensor (T_s), by ±25% of their original values. The graphical and numerical results are shown to demonstrate the AVR's tendency to respond to various operating scenarios. The numerical results for uncertainty, overshoot/undershoot, rise time, and error value for various uncertainties are provided in Tables 6-9.

TABLE 6. Robust response of AVR under ±25% change in T_a.

Parameter	Uncertainty (%)	Peak Overshoot/ Undershoot (%)	Rise Time (seconds)	ITSE
T_a	-25	1.17	0.35	0.001209
	+25	0.07	0.30	0.001456

TABLE 7. Robust response of AVR under ±25% change in T_e.

Parameter	Uncertainty (%)	Peak Overshoot/ Undershoot (%)	Rise Time (seconds)	ITSE
T_e	-25	0.07	0.35	0.001125
	+25	0.10	0.30	0.001577

Table 6 shows that the peak overshoot decreases from 1.17% to 0.07% when T_a is increased by 25%. This indicates that an increase in T_a results in a significantly reduced overshoot, which is favourable for system stability.

TABLE 8. Robust response of AVR under ±25% change in T_g.

Parameter	Uncertainty (%)	Peak Overshoot/ Undershoot (%)	Rise Time (seconds)	ITSE
Tg	-25	0.22	0.26	0.001299
	+25	0.40	0.35	0.001711

TABLE 9. Robust response of AVR under ±25% change in T_s.

Parameter	Uncertainty (%)	Peak Overshoot/ Undershoot (%)	Rise Time (seconds)	ITSE
Ts	-25	0.07	0.26	0.001406
	+25	0.07	0.3	0.001215

Conversely, a decrease in T_a leads to a higher overshoot, indicating that the system becomes less stable. The rise time decreases from 0.35 seconds to 0.30 seconds when T_a is increased by 25%. This reduction in rise time indicates that the system responds faster to changes in the reference signal with an increased T_a.

A decrease in T_a leads to a 0.05 second increase in the rise time. This is minimal but it does imply a marginally slower response. In both cases, the ITSE values of 0.001209 and 0.001456 respectively are quite low and are close to each other. This indicates that changes in T_a have a negligible impact on the steady-state performance of the SS0-3-DOF-PIDA system. The analysis reveals that the SSO-3-DOF-PIDA controlled AVR system is robust to variations in T_a. The system exhibits stable performance with minimal overshoot and good steady-state behaviour over a range of ±25% T_a variations.

The two scenarios with a ±25% change in T_e, are shown in Table 7, for the SSO-3-DOF-PIDA controlled AVR system. Both scenarios exhibit low peak overshoot values, with a slight increase from 0.07% to 0.10% when T_e is increased by 25%. This indicates that an increase in T_e leads to a minor increase in overshoot but maintains stable control. A decrease in T_e results in an extremely low overshoot. The rise time decreases from 0.35 seconds to 0.30 seconds when T_e is increased by 25%. This suggests that the AVR system responds slightly faster to changes in the reference signal when there is an increase in T_e . Conversely, a decrease in T_e results in a slightly longer rise time, indicating a slower response.

The ITSE values of 0.001125 and 0.001577 in both cases are close to each other and are low, indicating that changes in T_e have an insignificant impact on the steady-state performance of the AVR system. The system exhibits stable performance with very low overshoot and good steady-state behaviour over a range of ±25% T_e variations. This indicates that the SSO-3-DOF-PIDA controlled AVR system is robust to variations in T_e.

Table 8 shows that when T_g is increased by 25%, the peak overshoot increases marginally from 0.22% to 0.40%. Thus, an increase in T_g results in a slight increase in overshoot while maintaining steady control. A low overshoot is obtained with a drop in T_g. When T_g is raised by 25%, the rise time fluctuates between 0.26 and 0.35 seconds, staying within a constrained range. This shows that changes in T_g have a negligible effect on how quickly the AVR system reacts. The ITSE values of 0.001299 and 0.001711 are remarkably small, indicating that changes in T_g have a negligible effect on the steady-state performance of the AVR system. This demonstrates that the SSO-3-DOF-PIDA controlled AVR system is robust to variations in T_g. The system exhibits stable performance with minimal overshoot and satisfactory steady-state behaviour across a range of ±25% T_g variations.

The outcomes for sensor time variation T_s are detailed in Table 9. In both cases, the peak overshoot remains constant at 0.07%, indicating that the alterations in T_s, whether increased or decreased by 25%, do not significantly affect the peak overshoot, and the AVR system retains a low overshoot. The rise time changes by 0.04 seconds when T_s is increased or decreased by 25%, implying that changes in T_s have no impact on the rise time of the AVR system. The ITSE values of 0.001406 and 0.001215 in both situations are low and closely matched. This indicates that alterations in T_s have a negligible effect on the steady-state performance of the SSO-3-DOF-PIDA controlled AVR system. The system maintains stable performance with low overshoot and consistent steady-state behaviour over a range of ±25% T_s variations. The resilience of the SSO-3-DOF-PIDA-based AVR is further examined by modifying the time constants of the amplifier (T_a), exciter (T_e), generator (T_g), and sensor (T_s) by ±50% of their original values. The results of these modifications are recorded in Tables 10-13.

TABLE 10. Robust response of AVR under ±50% change in T_a.

Parameter	Uncertainty (%)	Peak Overshoot/ Undershoot (%)	Rise Time (seconds)	ITSE
T_a	-50	0.07	0.4	0.001169
	+50	0.07	0.35	0.001651

TABLE 11. Robust response of AVR under ±50% change in T_e.

Parameter	Uncertainty (%)	Peak Overshoot/ Undershoot (%)	Rise Time (seconds)	ITSE
T_e	-50	0.08	0.40	0.001051
	+50	0.21	0.34	0.001926

Table 10 presents two scenarios with a ±50% change in T_a for the SSO-3-DOF-PIDA controlled AVR system. In both scenarios the peak overshoot remains constant at 0.07%, indicating that changes in T_a have no impact on the peak overshoot. When T_a is increased by 50%, the rise time decreases by 0.05 seconds. Conversely, when T_a is decreased by 50%, the rise time increases by 0.05 seconds. The ITSE values in both cases are low at 0.001169 and 0.001651 and are close to each other, as was the result with a ±25% change in T_a. Based on these results it can be concluded that the SSO-3-DOF-PIDA controller provides robust control of the AVR system, maintaining stable and satisfactory performance even in the presence of substantial variations in T_a.

TABLE 12. Robust response of AVR under ±50% change in T_g.

Parameter	Uncertainty (%)	Peak Overshoot/ Undershoot (%)	Rise Time (seconds)	ITSE
T_g	-50	0.36	0.3	0.001681
	+50	1.07	0.4	0.002529

TABLE 13. Robust response of AVR under ±50% change in T_s.

Parameter	Uncertainty (%)	Peak Overshoot/ Undershoot (%)	Rise Time (seconds)	ITSE
T_s	-50	0.07	0.3	0.001511
	+50	0.06	0.35	0.001135

The results obtained when T_e is changed by ±50% are shown in Table 11. There is a low but noticeable difference in peak overshoot. When T_e is decreased by 50%, the peak overshoot increases to 0.21%, indicating greater overshoot, and when T_e is increased by 50%, the peak overshoot decreases to 0.08%. This suggests that changes in T_e have a negative impact on peak overshoot. The rise time also exhibits differences between the two scenarios. When T_e is increased by 50%, the rise time decreases from 0.40 seconds to 0.34 seconds. Conversely, when T_e is decreased by 50%, the rise time increases from 0.40 seconds to 0.34 seconds. These changes are consistent with the trend observed with a ±25% change in T_e. At 0.001051 and 0.001926, the ITSE values in both situations are comparatively low. Although the change in T_e has an impact on the ITSE value, the impact is minimal. ±50% change in T_e leads to noticeable differences in peak overshoot and rise time, which indicates that the SSO-3-DOF-PIDA controlled AVR system may be sensitive to drastic changes in T_e.

Under a ±50% change in T_g, the results in Table 12 demonstrate a noticeable difference in peak overshoot and rise time between the two states. When T_g is decreased the peak overshoot increases to 1.07%, and when T_g is increased, the peak overshoot decreases to 0.36%. This indicates that a significant decrease in T_g results in greater overshoot. Equally, a significant increase in T_g produces a lower overshoot. When T_g is increased or decreased, the rise time changes by 0.1 seconds. The trend in rise time changes is consistent with the results obtained under ±25% change in T_g. The change in T_g has a minimal impact on the steady-state performance of the system as indicated by the low ITSE values of 0.001681 and 0.002529.

TABLE 14. Response of AVR under ±50% change in forward gain (K_f).

Parameter	Uncertainty (%)	Peak Overshoot/ Undershoot (%)	Rise Time (seconds)	ITSE
K_f	-50	2.32	1.65	0.008248
	+50	0.58	0.28	0.001261

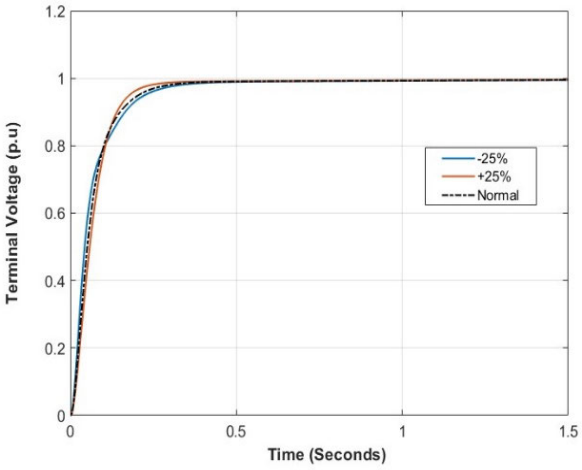

FIGURE 10. Response of terminal voltage under ±25% change in T_a.

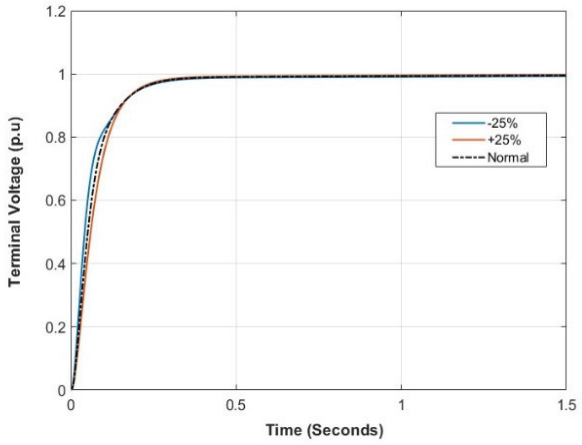

FIGURE 11. Response of terminal voltage under ±25% change in T_e.

In both scenarios indicated in Table 13, the results show that a change in T_s leads to minimal variations in peak overshoot, rise time, and the ITSE values, which aligns with the results observed earlier. This demonstrates that the controller can maintain consistent performance even when T_s undergoes significant changes.

The final robustness examination of the SSO-3-DOF-PIDA is undertaken by varying forward gain (K_f), which may be calculated as:

$$K_f = K_a \times K_e \times K_g \tag{29}$$

K_f is a parameter in the control system that represents the relationship between the control input and the system output under the steady state ($t \to \infty$). In essence, it indicates how

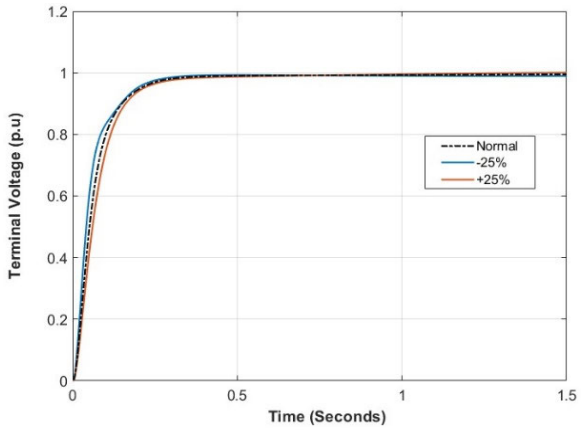

FIGURE 12. Response of terminal voltage under ±25% change in T_g.

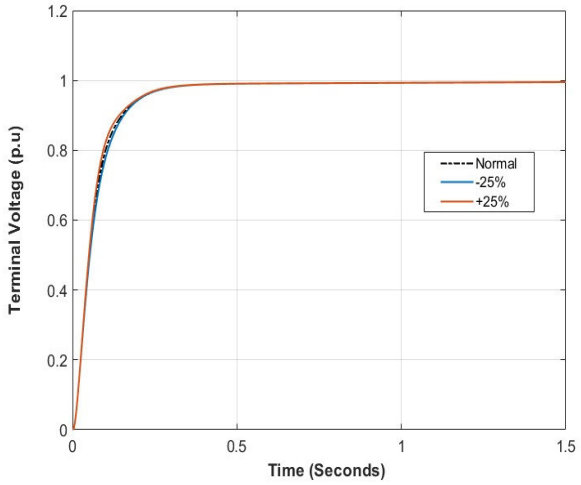

FIGURE 13. Response of terminal voltage under ±25% change in T_s.

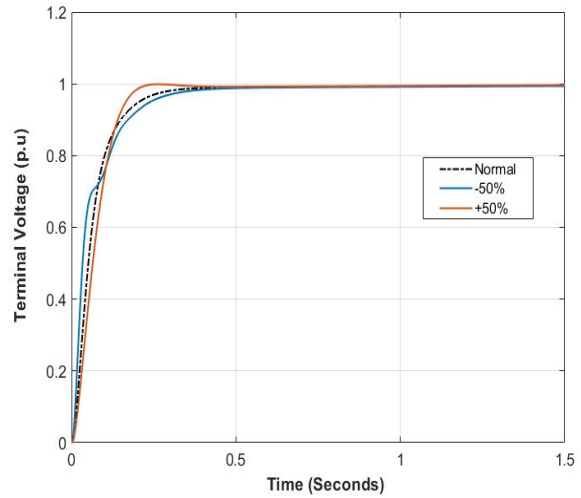

FIGURE 14. Response of terminal voltage under ±50% change in T_a.

sensitive the system is to changes in the input. The analysis is conducted under ±50% change in K_f, with the results shown in Table 14. When K_f is decreased by 50%, from − 50% uncertainty, the AVR system exhibits a peak overshoot

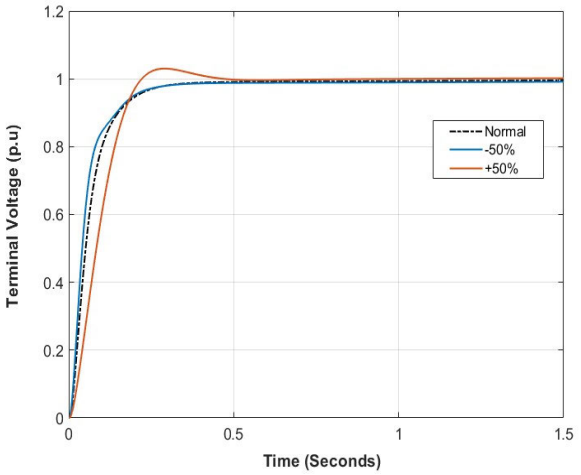

FIGURE 15. Response of terminal voltage under ±50% change in T_e.

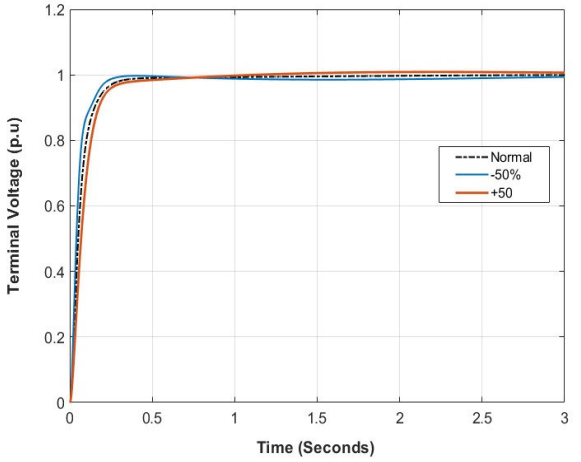

FIGURE 16. Response of terminal voltage under ±50% change in T_g.

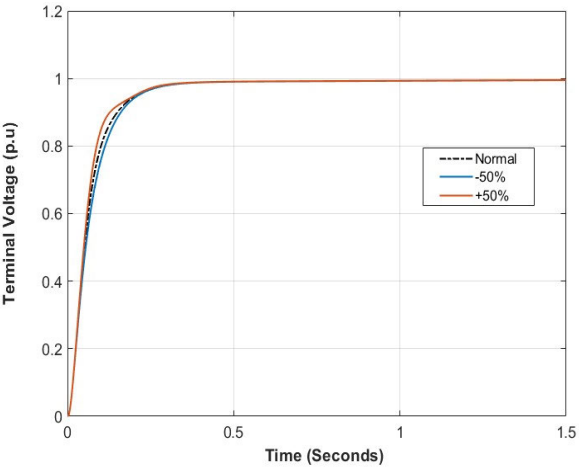

FIGURE 17. Response of terminal voltage under ±50% change in T_s.

of 2.32%. In contrast, when K_f is increased by 50%, from +50% uncertainty, the peak overshoot significantly decreases to 0.58%. This indicates that a higher K_f results in reduced peak overshoot. Similarly, when K_f is decreased by 50%,

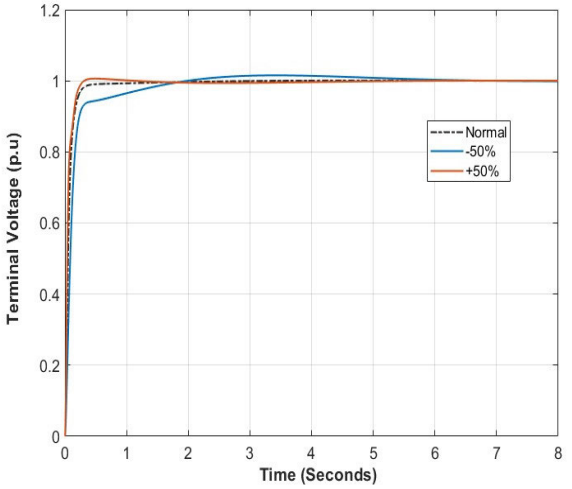

FIGURE 18. Response of terminal voltage under ±50% change in forward path gain (K_f).

the rise time increases to 1.65 seconds. However, when K_f is increased by 50%, the rise time decreases to 0.28 seconds. A higher K_f leads to a faster rise time. The ITSE value is significantly lower when K_f is increased by 50% compared to when it is decreased by 50%. This suggests that a higher K_f results in better overall control performance in terms of the ITSE values. The sensitivity analysis reveals that the SSO-3-DOF-PIDA-controlled AVR system exhibits different responses to changes in the K_f. A higher K_f results in reduced peak overshoot, faster rise time, and a lower ITSE value, indicating improved control performance. Conversely, a lower K_f leads to higher peak overshoot, slower rise time, and a higher ITSE value. The graphical results, presented in Fig. 10-18, confirm the analytical results, affirming the efficacy and promise of the SSO-3DOF-PIDA in producing robust control for the AVR framework. This is evident across a wide range of system parameter changes deviating from the reference values.

VI. CONCLUSION

This research aims to develop a robust automatic voltage regulation control strategy by integrating a 3-DOF-PIDA controller, a disturbance observer, and a SSO algorithm. The proposed control strategy's performance is assessed under non-linear uncertainties, parameter variations, and load disturbances, and compared with five commonly used controller designs.

Under normal operating conditions, the SSO-3-DOF-PIDA demonstrates robust control capabilities, with a minimal peak overshoot of 0.07%, rapid settling time of 0.5 seconds, minimal error accumulation of 0.001308, and the fastest rise time of 0.4 seconds. When subjected to a +30% voltage variation, the proposed strategy demonstrates its exceptional speed, accuracy, and resilience, with minimal overshoot, an impressive recovery time of 0.08 seconds and the lowest ITSE value of 0.01859, indicating a swift return to the desired voltage level, coupled with excellent steady-state

TABLE 15. 3-DOF-PIDA controller optimized parameters.

Parameter	Bounds	Optimized Values
K_p	[0.1, 2]	1.688369
K_i	[0.1, 2]	1.09614
K_d	[0.1, 2]	1.559584
K_{ac}	[0.01, 2]	0.1000689
K_l	[0.01, 1]	0.05889
α	[0.1, 1]	0.9999768
β	[0.1, 1]	0.9999995
γ	[0.1, 1]	0.2997942
N_d	[10, 1000]	492.495
N_a	[10, 1000]	265.1647

performance and minimal error accumulation. Furthermore, the inclusion of the disturbance observer in the control framework enhances the dynamic performance of the proposed strategy by effectively tracking real load disturbances, with negligible difference between the actual and estimated disturbance.

In the sensitivity analysis, the SSO-3-DOF-PIDA controlled AVR system consistently delivers robust performance, affirming its exceptional capabilities across diverse operating scenarios. Under ±25% parameter variations, the controller demonstrates its enhanced stability with a remarkable reduction in peak overshoot from 1.17% to an impressive 0.07% when increasing the amplifier and exciter time constants. Further, when the generator and sensor time constants are varied within ±25%, negligible effects are observed in the proposed control framework. Under ±50% parameter variations, the proposed strategy maintains its remarkable stability with insignificant control differences, emphasizing its adaptability to significant variations. A conclusive examination of the SSO-3DOF-PIDA control strategy is undertaken by varying the forward gain by ±50%. The results demonstrate the robustness and effectiveness of the SSO-3DOF-PIDA in providing stable AVR control.

The innovative integration of a 3-DOF-PIDA controller with a standard disturbance observer, embedded with the SSO, provides a unified and effective AVR control framework. The SSO simultaneously optimizes the parameters of the 3-DOF-PIDA controller and the disturbance observer, ensuring they work in harmony to achieve enhanced disturbance rejection and precise voltage regulation. Together, they provide superior voltage regulation performance by addressing dynamic operating conditions and external disturbances, which improves disturbance rejection, adaptability, and robustness in control systems, making this combination a valuable tool in AVR applications. In future work, the following may be considered:

- The observer may be optimized for the entire range of payload as well as the parameter variations for the total robust performance of the AVR under lumped disturbances.
- The investigations can be further extended by considering the frequency response analysis.
- The research work can be validated and investigated using hardware in loop utilizing OPAL-RT for various assorted operating conditions considering steady state and dynamic conditions.

APPENDIX

See Table 15.

REFERENCES

[1] R. C. Dorf and R. H. Bishop, *Modern Control Systems*, 13th ed. Boston, MA, USA: Pearson, 2016, ch. 12, pp. 854–916.
[2] M. Ćalasan, M. Micev, M. Radulović, A. F. Zobaa, H. M. Hasanien, and S. H. E. A. Aleem, "Optimal PID controllers for AVR system considering excitation voltage limitations using hybrid equilibrium optimizer," *Machines*, vol. 9, no. 11, p. 265, Oct. 2021, doi: 10.3390/machines9110265.
[3] K. J. Åström and T. Hägglund, "PID controllers: Theory, design, and tuning," *ISA Trans.*, vol. 42, no. 3, pp. 395–412, 1995.
[4] Ö. Can, C. Andiç, S. Ekinci, and D. Izci, "Enhancing transient response performance of automatic voltage regulator system by using a novel control design strategy," *Electr. Eng.*, vol. 105, no. 4, pp. 1993–2005, Mar. 2023, doi: 10.1007/s00202-023-01777-8.
[5] M. Milanesi, E. Mirandola, and A. Visioli, "A comparison between PID and PIDA controllers," in *Proc. IEEE 27th Int. Conf. Emerg. Technol. Factory Autom. (ETFA)*, Stuttgart, Germany, Sep. 2022, pp. 1–6, doi: 10.1109/etfa52439.2022.9921724.
[6] A. N. Karanam and B. Shaw, "A new two-degree of freedom combined PID controller for automatic generation control of a wind integrated interconnected power system," *Protection Control Modern Power Syst.*, vol. 7, no. 1, p. 20, Dec. 2022, doi: 10.1186/s41601-022-00241-2.
[7] P. Panda and A. K. Nanda, "Design and analysis of 3-DOF PID controller for load frequency control of multi area interconnected power systems," in *Proc. Int. Conf. Recent Innov. Electr., Electron. Commun. Eng. (ICRIEECE)*, Bhubaneswar, India, Jul. 2018, pp. 2983–2987, doi: 10.1109/ICRIEECE44171.2018.9009377.
[8] C. Naga Sai Kalyan, B. S. Goud, C. R. Reddy, M. Bajaj, and G. S. Rao, "SMES and TCSC coordinated strategy for multi-area multi-source system with water cycle algorithm based 3DOF-PID controller," *Smart Sci.*, vol. 11, no. 1, pp. 1–15, Mar. 2022, doi: 10.1080/23080477.2022.2054199.
[9] E. Sariyildiz, R. Oboe, and K. Ohnishi, "Disturbance observer-based robust control and its applications: 35th anniversary overview," *IEEE Trans. Ind. Electron.*, vol. 67, no. 3, pp. 2042–2053, Mar. 2020, doi: 10.1109/TIE.2019.2903752.
[10] R. V. Gandhi and D. M. Adhyaru, "Hybrid extended state observer based control for systems with matched and mismatched disturbances," *ISA Trans.*, vol. 106, pp. 61–73, Nov. 2020, doi: 10.1016/j.isatra.2020.06.019.
[11] R. Gandhi, D. Adhyaru, G. Sharma, and P. N. Bokoro, "Dual-extended state observer-based feedback linearizing control for a nonlinear system with mismatched disturbances and uncertainties," *Energies*, vol. 16, no. 7, p. 3142, Mar. 2023, doi: 10.3390/en16073142.
[12] R. Gandhi, S. B. Masikana, G. Sharma, and E. Çelik, "Design and robustness analysis of multiple extended state observer based controller (MESOBC) for AVR of the power system," *Int. Trans. Electr. Energy Syst.*, vol. 2023, pp. 1–15, Mar. 2023, doi: 10.1155/2023/1869840.
[13] V. Patel, D. Guha, and S. Purwar, "Optimized cascade fractional-order 3DOF-controller for frequency regulation of a hybrid power system using marine predators algorithm," *Int. J. Numer. Model., Electron. Netw., Devices Fields*, vol. 36, no. 5, May 2022, Art. no. e3025, doi: 10.1002/jnm.3025.
[14] A. Sivanandhan and V. Aneesh, "A review of optimisation algorithms used in proportional integral controllers (PID) for automatic voltage regulators," *ECS Trans.*, vol. 107, no. 1, pp. 5927–5934, Apr. 2022, doi: 10.1149/10701.5927ecst.

[15] A. R. Ibrahim, N. Basil, and M. I. Mahdi, "Implementation enhancement of AVR control system within optimization techniques," *Int. J. Nonlinear Anal. Appl.*, vol. 12, no. 2, pp. 2021–2027, Jul. 2021, doi: 10.22075/ijnaa.2021.5339.

[16] M. Micev, M. Ćalasan, and D. Oliva, "Design and robustness analysis of an automatic voltage regulator system controller by using equilibrium optimizer algorithm," *Comput. Electr. Eng.*, vol. 89, Jan. 2021, Art. no. 106930, doi: 10.1016/j.compeleceng.2020.106930.

[17] S. Oladipo, Y. Sun, and Z. Wang, "Optimization of PID and FOPID controllers with new generation metaheuristic algorithms for controlling AVR system: Concise survey," in *Proc. 12th Int. Conf. Comput. Intell. Commun. Netw. (CICN)*, Sep. 2020, pp. 280–286, doi: 10.1109/CICN49253.2020.9242585.

[18] A. M. Noman, S. Z. Almutairi, M. Aly, M. H. Alqahtani, A. S. Aljumah, and E. A. Mohamed, "A marine-predator-algorithm-based optimum FOPID controller for enhancing the stability and transient response of automatic voltage regulators," *Fractal Fractional*, vol. 7, no. 9, p. 690, Sep. 2023, doi: 10.3390/fractalfract7090690.

[19] P. Lakshmi, B. Venkateswara Rao, and R. Devarapalli, "BAT algorithm based optimal power flow for a power system consisting of wind power plant and static VAR compensator," in *Proc. Michael Faraday IET Int. Summit (MFIIS)*, Oct. 2020, pp. 7–12, doi: 10.1049/icp.2021.1081.

[20] B. Srikanth Goud, R. Reddy, M. Bajaj, V. N. Tulsky, and S. Kamel, "Fruit fly integration of plugin electric vehicles optimization technique based regulator for LFC of conventional power system with the, integration of plugin electric vehicles," in *Proc. 5th Int. Youth Conf. Radio Electron., Elect. Power Eng. (REEPE)*, Mar. 2023, pp. 1–6, doi: 10.1109/reepe57272.2023.10086898.

[21] J. Zhang, T. Zhang, G. Zhang, and M. Kong, "Parameter optimization of PID controller based on an enhanced whale optimization algorithm for AVR system," *Oper. Res.*, vol. 23, no. 3, Jun. 2023, Art. no. 44, doi: 10.1007/s12351-023-00787-5.

[22] A. M. Mosaad, M. A. Attia, and A. Y. Abdelaziz, "Comparative performance analysis of AVR controllers using modern optimization techniques," *Electr. Power Compon. Syst.*, vol. 46, nos. 19–20, pp. 2117–2130, 2018, doi: 10.1080/15325008.2018.1532471.

[23] R. K. Kuri, D. Paliwal, and D. K. Sambariya, "Grey wolf optimization algorithm based PID controller design for AVR power system," in *Proc. 2nd Int. Conf. Power Energy, Environ. Intell. Control (PEEIC)*, India, Oct. 2019, pp. 233–237, doi: 10.1109/PEEIC47157.2019.8976641.

[24] M. J. Blondin, J. Sanchis, P. Sicard, and J. M. Herrero, "New optimal controller tuning method for an AVR system using a simplified ant colony optimization with a new constrained Nelder–Mead algorithm," *Appl. Soft Comput.*, vol. 62, pp. 216–229, Jan. 2018, doi: 10.1016/j.asoc.2017.10.007.

[25] M. C. Rais, F. Z. Dekhandji, A. Recioui, M. S. Rechid, and L. Djedi, "Comparative study of optimization techniques based PID tuning for automatic voltage regulator system," *Eng. Proc.*, vol. 14, no. 1, p. 21, Feb. 2022, doi: 10.3390/engproc2022014021.

[26] S. Tiwari and A. Kumar, "Advances and bibliographic analysis of particle swarm optimization applications in electrical power system: Concepts and variants," *Evol. Intell.*, vol. 16, no. 1, pp. 23–47, Feb. 2023, doi: 10.1007/s12065-021-00661-3.

[27] M. S. Ayas and A. K. Sahin, "A reinforcement learning approach to automatic voltage regulator system," *Eng. Appl. Artif. Intell.*, vol. 121, May 2023, Art. no. 106050, doi: 10.1016/j.engappai.2023.106050.

[28] A. Rahman, L. C. Saikia, and N. Sinha, "Automatic generation control of an unequal four-area thermal system using biogeography-based optimised 3DOF-PID controller," *IET Gener., Transmiss. Distribution*, vol. 10, no. 16, pp. 4118–4129, Dec. 2016, doi: 10.1049/iet-gtd.2016.0528.

[29] P. K. Pathak, M. Jain, and A. K. Yadav, "Metaheuristic-assisted advanced control approach for time delayed unstable automatic voltage regulator," *Electric Power Compon. Syst.*, vol. 52, no. 2, pp. 173–188, Jan. 2024, doi: 10.1080/15325008.2023.2215793.

[30] M. Micev, M. Ćalasan, and M. Radulović, "Optimal tuning of the novel voltage regulation controller considering the real model of the automatic voltage regulation system," *Heliyon*, vol. 9, no. 8, Aug. 2023, Art. no. e18707, doi: 10.1016/j.heliyon.2023.e18707.

[31] E. Köse, "Optimal control of AVR system with tree seed algorithm-based PID controller," *IEEE Access*, vol. 8, pp. 89457–89467, 2020, doi: 10.1109/ACCESS.2020.2993628.

[32] S. Jung and R. C. Dorf, "Analytic PIDA controller design technique for a third order system," in *Proc. 35th IEEE Conf. Decis. Control*, Kobe, Japan, Feb. 1996, pp. 2513–2518 doi: 10.1109/CDC.1996.573472.

[33] A. M. Mosaad, M. A. Attia, and A. Y. Abdelaziz, "Whale optimization algorithm to tune PID and PIDA controllers on AVR system," *Ain Shams Eng. J.*, vol. 10, no. 4, pp. 755–767, Dec. 2019, doi: 10.1016/j.asej.2019.07.004.

[34] S. Alghamdi, H. F. Sindi, M. Rawa, A. A. Alhussainy, M. Calasan, M. Micev, Z. M. Ali, and S. H. E. Abdel Aleem, "Optimal PID controllers for AVR systems using hybrid simulated annealing and gorilla troops optimization," *Fractal Fractional*, vol. 6, no. 11, p. 682, Nov. 2022, doi: 10.3390/fractalfract6110682.

[35] M. Castelli, L. Manzoni, L. Mariot, M. S. Nobile, and A. Tangherloni, "Salp swarm optimization: A critical review," *Exp. Syst. Appl.*, vol. 189, Mar. 2022, Art. no. 116029, doi: 10.1016/j.eswa.2021.116029.

[36] L. Abualigah, M. Shehab, M. Alshinwan, and H. Alabool, "Salp swarm algorithm: A comprehensive survey," *Neural Comput. Appl.*, vol. 32, no. 15, pp. 11195–11215, Aug. 2020, doi: 10.1007/s00521-019-04629-4.

[37] Z. Belboul, B. Toual, A. Kouzou, L. Mokrani, A. Bensalem, R. Kennel, and M. Abdelrahem, "Multiobjective optimization of a hybrid PV/wind/battery/diesel generator system integrated in microgrid: A case study in Djelfa, Algeria," *Energies*, vol. 15, no. 10, p. 3579, May 2022, doi: 10.3390/en15103579.

[38] S. Ekinci, B. Hekimoglu, and S. Kaya, "Tuning of PID controller for AVR system using salp swarm algorithm," in *Proc. Int. Conf. Artif. Intell. Data Process. (IDAP)*, Sep. 2018, pp. 1–6, doi: 10.1109/IDAP.2018.8620809.

[39] I. A. Khan, A. S. Alghamdi, T. A. Jumani, A. Alamgir, A. B. Awan, and A. Khidrani, "Salp swarm optimization algorithm-based fractional order PID controller for dynamic response and stability enhancement of an automatic voltage regulator system," *Electronics*, vol. 8, no. 12, p. 1472, Dec. 2019, doi: 10.3390/electronics8121472.

[40] P. Sirsode, A. Tare, and V. Pande, "Design of robust optimal fractional-order PID controller using salp swarm algorithm for automatic voltage regulator (AVR) system," in *Proc. 6th Indian Control Conf. (ICC)*, India, Dec. 2019, pp. 431–436, doi: 10.1109/ICC47138.2019.9123188.

[41] S. Kumari and G. Shankar, "A novel application of salp swarm algorithm in load frequency control of multi-area power system," in *Proc. IEEE Int. Conf. Power Electron., Drives Energy Syst. (PEDES)*, Chennai, India, Dec. 2018, pp. 1–5, doi: 10.1109/PEDES.2018.8707635.

[42] P. Dey, A. Saha, P. Srimannarayana, A. Bhattacharya, and B. Marungsri, "A realistic approach towards solution of load frequency control problem in interconnected power systems," *J. Electr. Eng. Technol.*, vol. 17, no. 2, pp. 759–788, Oct. 2021, doi: 10.1007/s42835-021-00913-3.

[43] S. Mirjalili, A. H. Gandomi, S. Z. Mirjalili, S. Saremi, H. Faris, and S. M. Mirjalili, "Salp swarm algorithm: A bio-inspired optimizer for engineering design problems," *Adv. Eng. Softw.*, vol. 114, pp. 163–191, Dec. 2017, doi: 10.1016/j.advengsoft.2017.07.002.

[44] E. Çelik, N. Öztürk, and Y. Arya, "Advancement of the search process of salp swarm algorithm for global optimization problems," *Exp. Syst. Appl.*, vol. 182, Nov. 2021, Art. no. 115292, doi: 10.1016/j.eswa.2021.115292.

[45] S. A. El-Sattar, S. Kamel, M. Ebeed, and F. Jurado, "An improved version of salp swarm algorithm for solving optimal power flow problem," *Soft Comput.*, vol. 25, no. 5, pp. 4027–4052, Mar. 2021, doi: 10.1007/s00500-020-05431-4.

[46] R. A. El Sehiemy, F. Selim, B. Bentouati, and M. A. Abido, "A novel multi-objective hybrid particle swarm and salp optimization algorithm for technical-economical-environmental operation in power systems," *Energy*, vol. 193, Feb. 2020, Art. no. 116817, doi: 10.1016/j.energy.2019.116817.

[47] S. Dhawan, R. Gupta, A. Rana, and S. Sharma, "Various swarm optimization algorithms: Review, challenges, and opportunities," in *Soft Computing for Intelligent Systems*, N. Marriwala, C. C. Tripathi, S. Jain, and S. Mathapathi, Eds. Singapore: Springer, 2021, doi: 10.1007/978-981-16-1048-6_22.

NELSON DHANPAL CHETTY was born in Durban, South Africa, in 1973. He received the B.Tech. and M.Eng. degrees from the Department of Electrical Power Engineering, Durban University of Technology, South Africa. He is currently pursuing the Ph.D. degree with the Department of Electrical and Electronic Engineering, University of Johannesburg, South Africa. He is a Lecturer with the Department of Electrical Power Engineering, Durban University of Technology. His primary research interests include power system operation and control, renewable energy technology, and power system optimization techniques.

GULSHAN SHARMA (Member, IEEE) received the B.Tech., M.Tech., and Ph.D. degrees from renowned universities in India. He is currently a Senior Lecturer with the Department of Electrical Engineering Technology, University of Johannesburg. He has participated actively in several research projects and published more than 100 papers in prestigious international journals and reputable conferences. He holds a Y-rating as a Researcher from the National Research Foundation in South Africa. His academic focus revolves around power system operation and control, coupled with the application of artificial intelligence techniques to power systems. He is an accomplished scholar who serves as an Academic Editor for the *International Transactions on Electrical Energy Systems* (Hindawi) and an Academic Editor for *Journal of Electrical and Computer Engineering* (Hindawi).

RAVI GANDHI (Member, IEEE) was born in Ahmedabad, India, in 1984. He received the B.E. and M.Tech. degrees in instrumentation and control engineering from Nirma University, India, in 2006 and 2012, respectively, and the Ph.D. degree in control systems from Nirma University, in 2019, under the prestigious Visvesvaraya Fellowship. He was a Postdoctoral Researcher with Ghent University, South Korea, and IIT Gandhinagar, India, in 2019 and 2020. He is currently an Assistant Professor with the School of Engineering, Ajeenkya D. Y. Patil University, Pune, India. He has more than 15 years of experience in teaching, research, and industries. He is the author of more than 20 papers in reputed international journals and conferences. His research interests include non-linear system control, power systems, PID controllers, optimization, and intelligent control.

EMRE ÇELIK was born in Düzce, Turkey, in 1987. He received the Ph.D. degree in electrical and electronics engineering from Gazi University, in 2016. From 2011 to 2018, he was a Research Assistant with the Electric Machinery Laboratory, Gazi University. Since 2019, he has been an Associate Professor with the Electrical and Electronics Engineering Department, Engineering Faculty, Düzce University. He has participated actively in several research projects and published more than 100 papers in prestigious international journals and reputable conferences. His research interests include electric machinery and drives, control systems design, artificial intelligence, and power systems. According to the science-wide author databases of various performance indicators published by a collaboration of Stanford University and Elsevier, he is named in the world's top 2% of Scientists List for the third consecutive year.